Complete head cerebral sensitivity mapping for diffuse correlation spectroscopy using subject-specific magnetic resonance imaging models

MELISSA M. WU,[1] ^{ID} KATHERINE PERDUE,[2] SUK-TAK CHAN,[1]
KIMBERLY A. STEPHENS,[1] BIN DENG,[1] ^{ID} MARIA ANGELA
FRANCESCHINI,[1] AND STEFAN A. CARP[1],* ^{ID}

[1]*Athinoula A. Martinos Center for Biomedical Imaging, Massachusetts General Hospital, USA*
[2]*Thayer School of Engineering at Dartmouth, USA*
*stefan.carp@mgh.harvard.edu

Abstract: We characterize cerebral sensitivity across the entire adult human head for diffuse correlation spectroscopy, an optical technique increasingly used for bedside cerebral perfusion monitoring. Sixteen subject-specific magnetic resonance imaging-derived head models were used to identify high sensitivity regions by running Monte Carlo light propagation simulations at over eight hundred uniformly distributed locations on the head. Significant spatial variations in cerebral sensitivity, consistent across subjects, were found. We also identified correlates of such differences suitable for real-time assessment. These variations can be largely attributed to changes in extracerebral thickness and should be taken into account to optimize probe placement in experimental settings.

1. Introduction

Diffuse correlation spectroscopy (DCS) is a non-invasive optical technique for continuous measurement of blood flow that is rapidly becoming established in the field [1,2]. In DCS, the intensity fluctuations of multiply scattered near-infrared light illuminating a tissue sample are employed to quantify red blood cell movement within the region of interest [3]. This technology is especially valuable for neuromonitoring, where accurate, continuous assessment of cerebral blood flow (CBF) is desired across a variety of circumstances [2]. In particular, for adults, DCS has shown success in understanding the impact of supplemental perfusion strategies during surgeries requiring cardiac arrest [4]; in the prolonged monitoring and CBF assessment for brain-injured patients in the neurocritical care unit [5–11]; in measuring brain hemodynamics during clinical interventions for acute stroke patients [12–15]; in elucidating CBF responses in patients with sleep apnea [16]; and in identifying cerebral autoregulation failure in patients with cardiovascular disease [17]. Such studies demonstrate potential for bedside or surgical CBF management for various conditions to allow for individualized care and treatment. Outside the clinic, DCS has been implemented in basic neuroscience applications such as disease-specific or functional studies [18–22], and its utility is likely to become more widespread with increasing technological advancements [20,23–28].

For practical purposes – due to the presence of hair – nearly all neuromonitoring applications so far have involved placing a DCS probe on the forehead for CBF characterization in the prefrontal cortex [1]. However, available locations for probe placement can be limited by other monitoring equipment, such as electroencephalography electrodes (EEG) [4], and it is often difficult to assess whether adequate brain signal has been acquired [2,29]. Specific areas on the head with high expected cerebral sensitivity that are best suited for DCS measurements, along

with surrogate markers thereof, have not been explicitly identified. Previous studies that have investigated cerebral sensitivity variations across the head for similar diffuse optical methods such as near-infrared spectroscopy (NIRS) have found significant variations in cerebral signal effected by anatomical differences such as extracerebral thickness and surface folds in the cerebral cortex [30–33]. Such studies, however, have either sampled magnetic resonance imaging (MRI) information from children or infants, or have focused their analyses on a single adult head. Cerebral sensitivity variations, both inter-subject and spatial, pertaining to application of DCS neuromonitoring in adults remain unknown despite these NIRS studies, because 1) the adult population has not been meaningfully sampled for comprehensive DCS sensitivity mapping, and 2) cortical sensitivity and resistance to extracerebral contamination are expected to be higher and more non-linear for DCS than for NIRS due to both the higher cerebral to extra-cerebral blood flow ratio versus the cerebral to extra-cerebral hemoglobin concentration ratio, and due to the physics of light-field decorrelation [34]. Thus, while we expect the anatomical variations in NIRS studies to also be seen in the DCS sensitivity maps, the specific patterns remain an open question. Mapping areas of high cerebral sensitivity and their corresponding brain regions can aid in optimizing DCS probe placement, which would not only benefit clinical neuromonitoring applications, but would also be advantageous in basic science studies. For completeness, we map the cerebral sensitivity across the entire head, as solutions developed in the fNIRS field for measurements could in the future be applied for DCS perfusion monitoring as well.

In this work, we characterize whole head DCS cerebral sensitivity using sixteen subject-specific head models derived from magnetic resonance imaging (MRI) structural scans. Some eight hundred evenly spaced points of interest were placed on the surface of each subject volume, along with a virtual light source and several detectors for each point. A mesh-based Monte Carlo light propagation simulation was run for each location, and cerebral sensitivity was calculated as the recovered CBF change from a simulated increase in brain blood flow. Other physiological parameters, such as scalp and skull thickness, were also calculated for each point. Correlate measures of cerebral sensitivity, along with inter- and intra-subject variation, were additionally investigated. The results were then statistically analyzed and integrated to form final recommendations on optimizing DCS probe placement in experimental contexts.

2. Methods

2.1. MRI acquisition

Sixteen subjects underwent MRI scans as part of a larger study approved by the Mass General Brigham Institutional Review Board, and each subject provided written consent prior to imaging. A multi-echo MPRAGE T1-weighted scan was acquired for each subject, and basic subject characteristics are tabulated in Table 1.

Table 1. Subject information.

	Number	Age (average ± standard deviation)
Total subjects	16	29 ± 5 years
Total female subjects	12	29 ± 5 years
Total male subjects	4	30 ± 3 years

The age range of the subjects was between 25 and 41 years. Racial and ethnic demographics are as follows: two subjects identified as Black/African-American, two as Asian, two as "more than one race", and the rest as White. Two subjects identified as Hispanic/Latino, one as unknown, and the rest as non-Hispanic or Latino.

2.2. Image segmentation and probe placement

Initial processing and segmentation of each structural T1 image was performed with the FreeSurfer software "recon-all" functionality [35]. The resulting white matter and subcortical segmentations, along with the original T1 and "brain mask" (the T1 image stripped of the skull and dura) were then inputted into a T1 segmentation algorithm written by Perdue et al. to generate a five-layer volume consisting of the scalp, skull, cerebrospinal fluid (CSF), grey matter, and white matter [36]. This volume was then transformed into a five-layered head mesh via the "v2m" function in the iso2mesh toolbox [37,38]. We chose to use a mesh rather than a traditional volume representation because of demonstrated improvements in mesh-based Monte Carlo photon simulations for curved-boundary structures [39], which is particularly important in this study to accurately model the effects of the cortical sulci and gyri. In generating the mesh from the segmented volume, the target maximum edge length of the surface triangles was 5 mm, and the target maximum volume of the tetrahedral elements was 200 mm^3. Of note, simulations were also tested on a single subject mesh with max. edge length and element volume of 2 mm and 100 mm^3 respectively; significant differences were not found in the cerebral sensitivity results between this finer mesh and the coarser one (with max. edge length and element volume 5 mm and 200 mm^3) of the same subject. Mesh characteristics for the subjects were as follows: the number of nodes for each subject averaged 214,529 with a standard deviation of 19,007, a minimum of 184,693 and a maximum of 274,312. The number of elements for each subject averaged 1,295,216 with a standard deviation of 114,330, a minimum of 1,115,691 and a maximum of 1,660,102. For an example subject with 214,005 nodes, the mean node edge length was 2.87 mm with a standard deviation of 1.67 mm. Across all subjects, the average mean node edge length was 2.88 mm, and the standard deviation of the mean node edge length was 0.05 mm.

In order to define consistent sensitivity locations of interest across a variety of head surface anatomies, a custom point-placement system was developed to create a high-density sensitivity location map for each subject. This custom point-placement system was inspired by the international 10/20 EEG system [40], but affords a much higher number of sensitivity sampling locations, which is desired for this study. First, five reference points were manually identified on each head: the nasion, a bone depression between the eyes on the nose bridge; the inion, a protrusion of the occipital bone at the back of the skull; the head center, which was approximated as the midpoint between the nasion and the inion (near the top of the head); the left ear point, chosen where the outer ear helix meets the skull; and the right ear point, the right-side analog of the left ear point. Points were placed separately for the anterior and posterior sides of the head. For the anterior side, a line across the forehead was drawn connecting the nasion to the head center using the "qmeshcut" functionality in iso2mesh [37], and we refer to this line as the "sagittal line". Similarly, a second line was drawn along the top of the head connecting the right ear point, head center, and left ear point; this will be referred to as the "coronal line". Figure 1(a) shows the construction of the coronal and sagittal plane outlines.

The sagittal line was then reduced to nineteen equally spaced points, including the nasion and the head center, and the coronal line was similarly reduced to thirty-seven equally spaced points, including the right and left ear points and the head center. Figure 1(b) shows this reduction from the outlines into points. These numbers of points were chosen to achieve an approximate 8-9 mm spacing between points.

Afterward, an initial line was drawn along the head connecting the right ear point, nasion, and left ear point. A second line was drawn connecting the points nearest the right ear point, nasion, and left ear point, respectively; a third line was drawn in a similar manner connecting the second-nearest points to the three reference points. This process was repeated until lines were drawn through all points in the sagittal line except for the head center. Each line was then reduced to a number of equally spaced points (approximately 7-9 mm interpoint spacing) which was determined by its location on the head – lines closer to the nasion contained more points
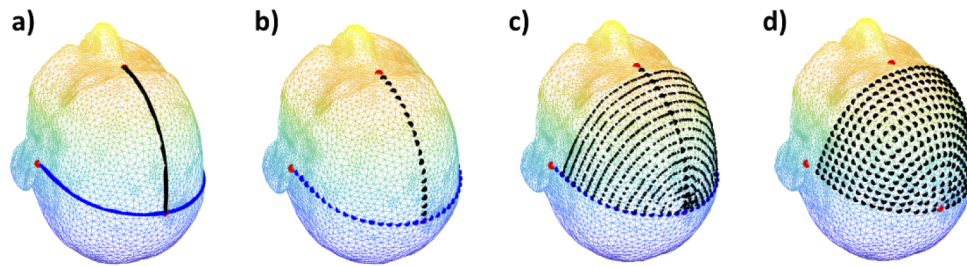
Fig. 1. : a) The sagittal line (black) and the coronal line (blue). The nasion, head center, and left ear reference points are shown in red. b) Reduced sagittal and coronal lines. c) Lines are drawn connecting two points from the coronal line and one point from the sagittal line. d) Connecting lines are reduced to points.

while lines closer to the head center had fewer. The reduced points were then refined by manually adjusting any points that were poorly placed from the automated algorithm. Finally, the lowest front line containing the nasion and the front line just above it was removed after point placement because they ran through the eyes or eyebrows. Figure 1(c) and 1(d) show the initial lines and the final point placement on the anterior side of the head.

Point placement for the posterior side of the head was performed analogously, with the nasion reference point being replaced by the inion. No final lines were removed in the posterior side, and the combined point placement for an example subject, resulting in a total of eight hundred and seventeen points, is shown in Fig. 2(a) and 2(b).
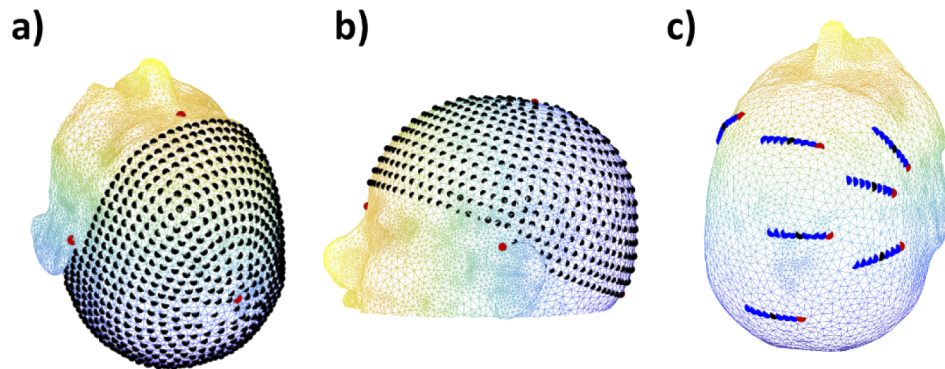

Fig. 2. a) Final point placement for an example subject, top view. b) Final point placement for same subject, side view. c) Placement of the virtual 1-source 8-detector probes. Sources are red points while detectors are blue points. The sensitivity locations, located at the midpoint of a probe, are shown in black.

Virtual sources and detectors were placed at each sensitivity point, in an orientation similar to typical *in-vivo* experiment setups in the forehead region (for consistency, this orientation was kept the same in other areas of the head, though they have not been measured as much), and were done as follows. A line connecting the right and left ear points and the sensitivity point of interest made along the top of the head (again with the aforementioned "qmeshcut" functionality). The source was placed 20 mm from the sensitivity point toward the right ear point (measured along the line following the curved head geometry, and not the Euclidean distance), and eight detectors were placed along the line from 5 to 40 mm away from the source in 5 mm increments. Thus, each sensitivity point was the midpoint between a source and the corresponding 40 mm detector. Figure 2(c) shows sample source and detector placements for an example subject.

2.3. Monte Carlo simulations and sensitivity calculations

A mesh-based Monte Carlo light propagation simulation, developed by Fang et al. [41], was run on each probe location (centered on each sensitivity point) for every subject using the source and detector locations detailed above. The vast majority of the simulations were run on NVIDIA Quadro RTX6000 and RTX8000 graphics processing units provided by the Massachusetts Life Sciences Cluster at the Massachusetts General Hospital Martinos Center for Biomedical Imaging. One and a half billion photons were launched per simulation; for simulation efficiency, detector sizes were adjusted such that 150-200 thousand photons were detected per detector while maintaining no greater than a 5% deviation from the intended source-detector (s-d) distance. This resulted in detector radii of 0.13, 0.28, 0.45, 0.7, 1, 1.5, 1.75, and 2 mm for the 5-, 10-, 15-, 20-, 25-, 30-, 35-, and 40-mm detectors, respectively. Each simulation took approximately 20-40 minutes to run. Optical properties for each tissue layer, consistent with an 850 nm source and taken from Gagnon et al. [42], are displayed in Table 2.

Table 2. Optical properties at 850 nm used for the Monte Carlo light propagation simulations.

	Reduced scattering, mm^{-1}	Absorption, mm^{-1}
Scalp	0.74	0.0164
Skull	0.81	0.0115
CSF	0.01	0.0017
Grey matter	1.16	0.017
White matter	1.16	0.017

The outputs of the simulations were then post-processed to generate simulated DCS data, i.e., intensity autocorrelations, for three different physiological states: baseline, increased cerebral blood flow, and decreased scalp blood flow. To do so, photon path lengths and momentum transfers were saved from each simulation, and this information was used as inputs into the temporal field autocorrelation function calculation [43]:

$$G_1(\tau) = \frac{1}{N_p} \sum_{n=1}^{N_p} exp\left(-\frac{1}{3}k_0^2 \sum_{i=1}^{N_t} Y_{n,i} r^2(\tau)_i \right) \ exp\left(-\sum_{i=1}^{N_t} \mu_{a,i} L_{n,i} \right) \tag{1}$$

where k_0 is the wavenumber of the light in the medium, N_p is the number of photons detected, N_t is the number of tissue layers, $Y_{n,i}$ is the total momentum transfer of photon n in layer i, $L_{n,i}$ is the total path length of photon n in layer i, $\mu_{a,i}$ is the absorption coefficient in layer i, and $\langle \Delta r^2(\tau) \rangle_i$ is the mean square displacement of the red blood cells (assumed to dominate dynamic scattering) in tissue i at time delay τ, given by

$$\langle \Delta r^2(\tau) \rangle = 6BF_i\tau \tag{2}$$

where BF_i is the blood flow index. The source wavelength used was 850 nm. The input BF_i values for the different physiological states, estimated from previous *in-vivo* DCS measurements (data not published), are shown in Table 3 (physiological variations of 50% in either the scalp or the brain layers were simulated in this study).

Finally, the normalized temporal autocorrelation function was then calculated as:

$$g_2(\tau) = 1 + \beta(g_1(\tau))^2; \ g_1(\tau) = \frac{G_1(\tau)}{\langle I \rangle} \tag{3}$$

where g_1 is the normalized electric field temporal autocorrelation, β is the coherence factor dependent on the system characteristics, and I is the average photon fluence. A coherence factor

Table 3. Input BF$_i$ values for the three different physiological states.

	Baseline BF$_i$, mm^2/s	Increased CBF state BF$_i$, mm^2/s	Decreased scalp flow state BF$_i$, mm^2/s
Scalp	10^{-6}	10^{-6}	$\mathbf{5 \times 10^{-7}}$
Skull	2×10^{-8}	2×10^{-8}	2×10^{-8}
CSF	5×10^{-8}	5×10^{-8}	5×10^{-8}
Grey matter	6×10^{-6}	$\mathbf{9 \times 10^{-6}}$	6×10^{-6}
White matter	6×10^{-6}	$\mathbf{9 \times 10^{-6}}$	6×10^{-6}

of 0.5 was assumed, and the resulting g_2 function for each detector and physiological state was used as the simulated DCS data.

To process the simulated data, each g_2 autocorrelation was then fit for BF$_i$ at each source-detector separation using the analytical solution to the semi-infinite diffusion correlation equation [43]:

$$G_1(\rho, \tau) = \frac{3\mu_s{}'}{4\pi} \left[\frac{\exp(-Kr_1)}{r_1} - \frac{\exp(-Kr_2)}{r_2} \right] \tag{4}$$

With

$$K^2 = 3\mu_a\mu_s{}' + \mu_s{}'^2 k_0^2 \alpha \langle \Delta r^2(\tau) \rangle \tag{5}$$

where $G_1(\rho, \tau)$ is the electric field autocorrelation function at a source-detector separation ρ and delay time τ, $\mu_s{}'$ is the reduced scattering coefficient, μ_a is the absorption coefficient, k_0 is the wavenumber of light in the medium, α is the probability of scattering from a moving scatterer, ρ is the source-detector separation, $r_1 = (\rho^2 + z_0^2)^{1/2}$, and $r_2 = (\rho^2 + (z_0 + 2z_b)^2)^{1/2}$, with $z_0 = \mu_s{}' - 1$, and $z_b = 1.76/\mu_s{}'$ for a tissue index of refraction of 1.37. The analytical g_1s were converted to g_2s using Eq. (3). The g_2 decays were fit for autocorrelation lags from 10^{-7} to 10^{-2} seconds, and the lsqcurvefit function in MATLAB 2021a (MathWorks, Natick, MA) was used to fit the simulated data with BF$_i$ and β as parameters.

Cerebral sensitivity was calculated as the fraction of the recovered increase in BF$_i$ compared to the 50% ground truth CBF increase. For example, if a 30% increase in BF$_i$ was detected given the 50% ground truth CBF increase, then the cerebral sensitivity was calculated as 60%. Likewise, scalp sensitivity was defined as the percentage observed decrease in BF$_i$ from a 50% decrease in scalp blood flow; if a 30% reduction from baseline BF$_i$ was observed given a 50% decrease in scalp blood flow, then scalp sensitivity was calculated as 60%. In general, high levels of cerebral sensitivity and low levels of scalp sensitivity are desirable for CBF measurements. The ratio of long s-d separation BF$_i$ to short s-d separation BF$_i$ at the baseline physiological state was also calculated. For locations of higher cerebral sensitivity, the weighting of the brain dynamics in the apparent BF$_i$ will be higher, thus we expect higher BF$_i$ values at these locations since blood flow in the brain is higher than in the scalp [44]. Thus, the long s-d separation BF$_i$ values (and hence the ratio metric) are expected to be higher for locations of higher cerebral sensitivity. Fluence values at each detector were not saved due to preliminary investigations showing little correlation with sensitivity (not shown).

2.4. Other processing and group analyses

Distance to the skull, CSF, and brain at each sensitivity point was calculated; the first two were computed to calculate scalp, skull, and CSF thickness. The segmented 3-D head volume (and not the head mesh) was used to calculate the Euclidean distances from each of the skull, CSF, and grey matter voxels, respectively, to the sensitivity point in question. The scalp thickness was defined as the distance between the sensitivity point and the nearest skull voxel. The distance to CSF was defined as the distance between the sensitivity point and the nearest CSF voxel; the skull thicknesses were calculated as the scalp thickness subtracted from the distance to CSF.

Likewise, the distance to the brain (and thus total extracerebral thickness) was defined as the distance between the sensitivity point and the nearest grey matter voxel, and the CSF thicknesses were calculated as the distance to CSF subtracted from the total extracerebral thickness.

Group analyses were also performed. Since each subject had sensitivity points of interest defined relative to landmarks on the head surface, cerebral sensitivity values for each location were directly averaged across subjects. Separate estimates of the average for the male versus female subjects were also calculated. Similar analyses were performed for the distance to brain at each sensitivity point. The fourteen points nearest to each ear were removed for lack of accuracy in source-detector placement, as some detectors would fall on the ears. For visualization purposes, group average values were displayed on the mesh of the Colin27 head [45], although no simulations were run on the Colin27 volume itself. Surface plots of group average values were constructed from the 3-D sensitivity points using a MATLAB triangulation function [46], and plotted using the "trisurf" MATLAB functionality.

Ordinary least squares regression was performed to correlate cerebral sensitivity with extracerebral thickness, photon penetration through brain tissue, scalp sensitivity, and ratio of long s-d separation baseline BF_i to short s-d separation baseline BF_i. To calculate the photon penetration through brain tissue, the photon path lengths (obtained from the Monte Carlo simulation output) through the grey and white matter tissues was divided by the total photon path lengths for each detector.

3. Results

3.1. Group averages of sensitivity and tissue thickness across the head

Figure 3 shows the group average cerebral sensitivity across the sixteen subjects. The average cerebral sensitivity increases with s-d distance, as expected. High sensitivity is observed at the lateral sides of the forehead, at the temporal bone areas, and at the occipital bone area for all s-d distances. Low sensitivity is observed at the crown of the head. On the forehead, there is slightly higher sensitivity on the subject left side than the right side; at the back of the skull, there is slightly higher sensitivity on the subject right side than the left side. Table 4 shows the minimum and maximum of the group average cerebral sensitivities for each s-d separation – i.e., the group average cerebral sensitivity at each location was calculated from all subjects (as in Fig. 3), and the minimum and maximum values across all locations were recorded. On the other hand, Table 5 shows the average minimum and maximum cerebral sensitivity values across all subjects – in other words, the minimum and maximum sensitivities across the head were calculated for each subject, and these min. and max. values were subsequently averaged together. The standard deviation in the table is calculated likewise.

Table 4. Minimum and maximum of the group average cerebral sensitivities per s-d separation.

	Minimum of average cerebral sensitivity	Maximum of average cerebral sensitivity
25 mm	3.92%	39.70%
30 mm	8.32%	52.46%
35 mm	16.16%	61.76%
40 mm	26.46%	68.20%

We note that the maximum average recovered increase in CBF exceeds 50% of the ground truth increase in CBF only at s-d separations of approximately 30 mm and higher. To illustrate inter-subject variability, Fig. 4 displays individual cerebral sensitivity plots in five example subjects at an s-d separation of 30 mm.

Subject 1 (female) shows the lowest cerebral sensitivity across the head, but is included as an example where the lower back of the head displays a higher cerebral sensitivity than on the
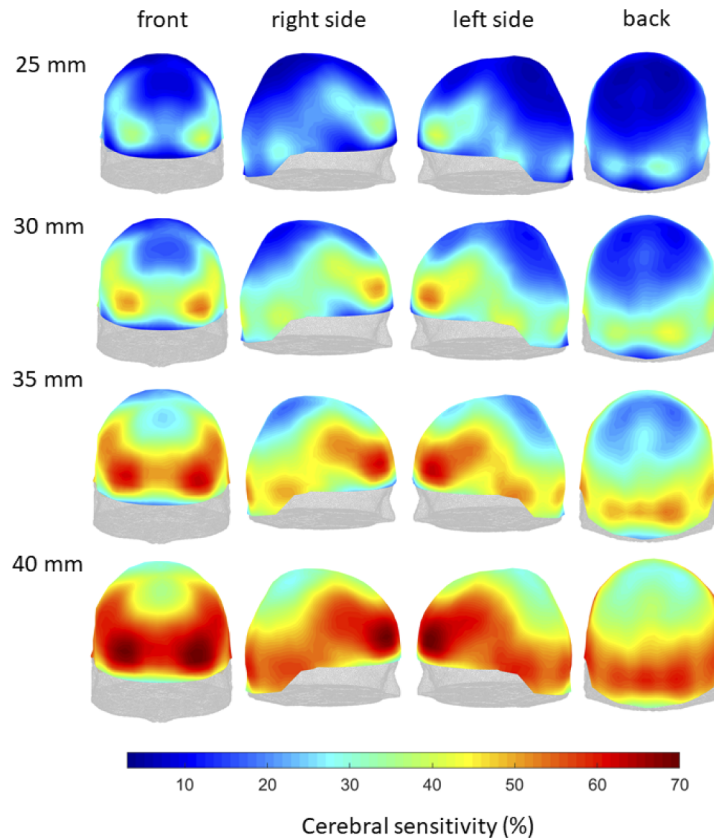
Fig. 3. Group average cerebral sensitivity values plotted for s-d distances between 25- and 40-mm. Sensitivity is defined as the recovered percentage increase in CBF from a ground truth increase of 50%.

Table 5. Min. and max. sensitivities across the head were calculated individually for each subject, and then averaged across all subjects. Standard deviation was also calculated.

	Mean and standard deviation of the subjects' minimum cerebral sensitivities	Mean and standard deviation of the subjects' maximum cerebral sensitivities
25 mm	$1.14 \pm 1.46\%$	$49.70 \pm 13.96\%$
30 mm	$2.72 \pm 3.34\%$	$60.52 \pm 11.04\%$
35 mm	$5.6 \pm 6.18\%$	$67.60 \pm 8.86\%$
40 mm	$9.74 \pm 9.84\%$	$72.72 \pm 7.28\%$

forehead. Subject 2 (male) displays a sensitivity profile reflective of what is observed in the group average sensitivity plot. The plot for subject 3 (female) is similar, and contains high sensitivity not only on the lateral sides of the forehead but in the middle of the forehead as well. Subject 4 (female) shows the same phenomenon, and increased sensitivity on the lateral sides further up toward the crown of the head. A high degree of sensitivity asymmetry near the occipital bone is also shown in subject 4. Last, subject 5 (female) shows the most cerebral sensitivity, again with increased sensitivity on the lateral sides nearer the crown of the head, along the temporal bone, and on the occipital bone area.
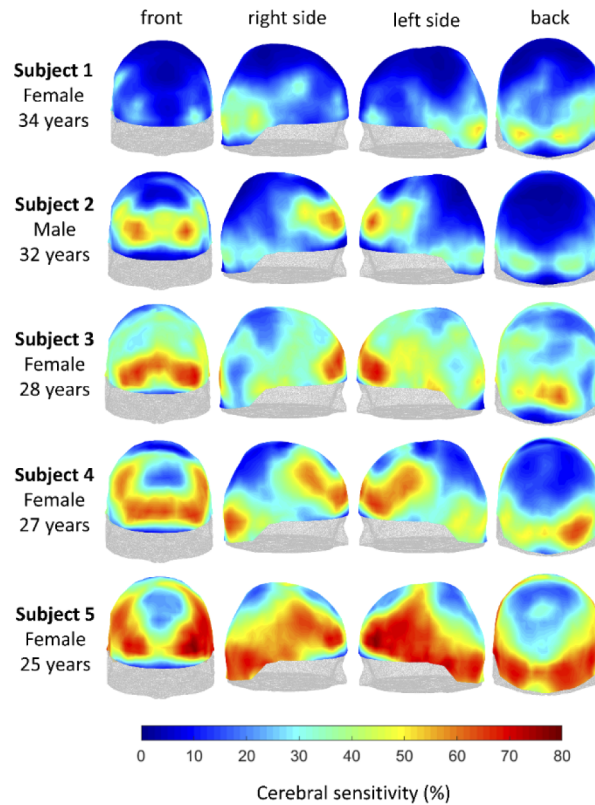
Fig. 4. Cerebral sensitivity surface plots at 30-mm detector distance for five subjects.

Figure 5 compares the average cerebral sensitivity in the female subjects (n=12) and the male subjects (n=4) for the 30 mm s-d separation. The cerebral sensitivity patterns match what is observed in the group average. For the females, the average sensitivity ranges from 9.52% to 57.14%, whereas for the males, the average sensitivity ranges from 2.18% to 45.10%. To compare the two subgroups, the sensitivity values across the entire head (for the 30 mm s-d separation) were averaged for each individual subject. This resulted in twelve spatial average values for the female subjects and four spatial average values for the male subjects. There was no significant difference between groups based on a Kruskal-Wallis test (p=0.116); however, due to the small sample sizes, the power of the test is limited, and results may not be representative of a larger sample size. Further data is likely needed for robust comparison between sexes.

Figure 6 shows the average extracerebral thickness across female subjects, male subjects, and all subjects. Low extracerebral thickness is observed at the forehead, lower back of the head, and the temporal sides of the head; high extracerebral thickness is observed at the crown of the head. For female subjects, the average distance to brain ranged from 11.11–20.61 mm, whereas for male subjects, the average distance to brain ranged from 11.56–24.63 mm. Across all subjects, the average distance to brain ranged from 11.32–21.22 mm. As before, the extracerebral thickness across the entire head was averaged for each individual subject, with twelve spatial average values for the females and four spatial average values for the males. The difference was significant based on a Kruskal-Wallis test (p<0.03), but again, the statement in the previous paragraph regarding sample sizes is relevant here as well.
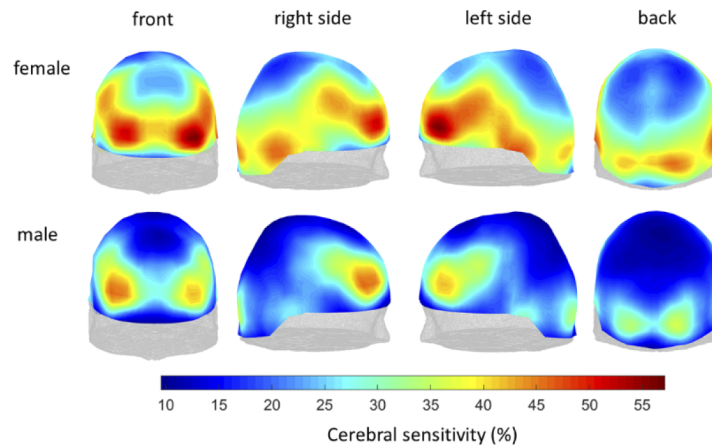
Fig. 5. Average female cerebral sensitivity and average male cerebral sensitivity at the 30 mm s-d separation.
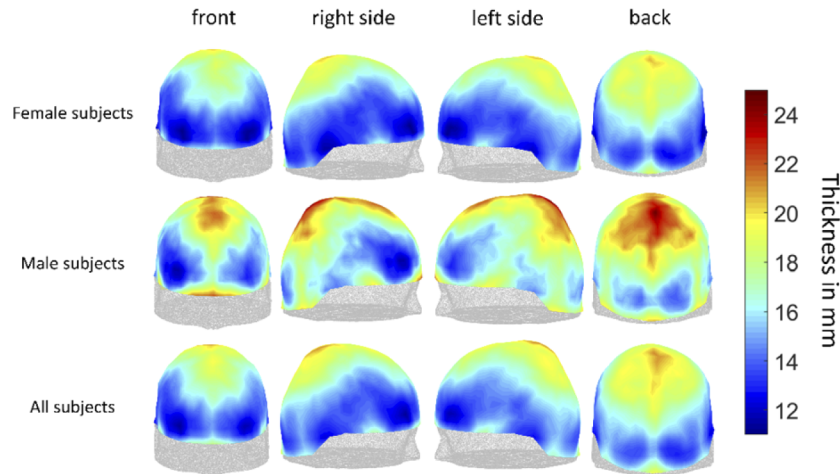

Fig. 6. Average extracerebral thickness for female, male, and all subjects.

Table 6 displays the approximate observed thicknesses of each tissue layer for different regions on the head over all subjects. In terms of total distance to the brain, the parietal area is generally the least favorable for DCS measurements.

Table 6. Approximate observed thicknesses (mean ± standard deviation) of each tissue layer per region on head. All units are in mm.

	Frontal	Temporal	Parietal	Occipital
Scalp	6.85 ± 1.08	9.85 ± 1.78	8.87 ± 1.76	8.84 ± 1.83
Skull	6.35 ± 2.68	3.47 ± 1.62	7.17 ± 1.86	4.67 ± 2.14
CSF	2.74 ± 1.99	2.44 ± 1.80	2.44 ± 1.75	2.72 ± 2.14
Total distance to brain	14.79 ± 2.87	14.45 ± 2.37	17.30 ± 2.57	14.80 ± 2.73

3.2. Determinants of cerebral sensitivity

In the following two sections, we display analyses with data across all subjects and all locations, but with only the 30 mm s-d separation, as the results for the other detector distances are similar. Figure 7 shows a binned scatter plot of cerebral sensitivity versus distance to brain across all subjects and all sensitivity locations for a s-d distance of 30 mm. Ordinary least squares regression shows that 75% of the variance in cerebral sensitivity can be attributed to changes in the extracerebral thickness.
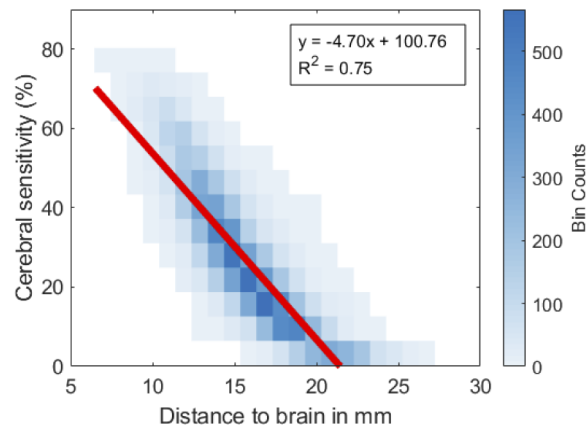

Fig. 7. A binned scatter plot of cerebral sensitivity at 30 mm versus distance to brain. Ordinary least squares regression reveals that 75% of the variation in cerebral sensitivity can be explained by the total extracerebral thickness.

Figure 8 shows the fraction of photon pathlength through brain tissue versus the distance to brain for a s-d distance of 30 mm. The penetration into the brain decreases approximately linearly with increasing extracerebral thickness, again with 75% of the variance in brain penetration explained by variance in extracerebral distance.
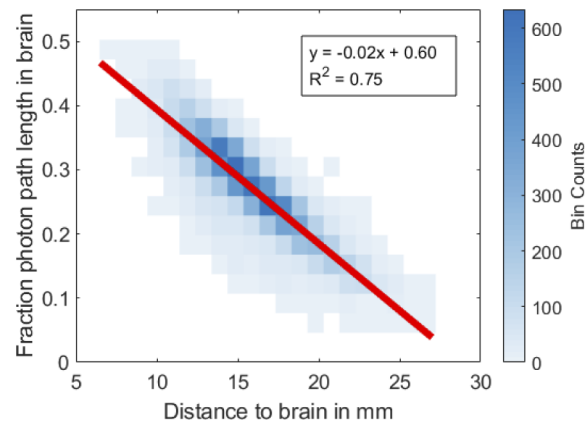

Fig. 8. The fraction of photon path length in the brain versus distance to the brain at 30 mm. The relationship is approximately linear.

Figure 9 shows the cerebral sensitivity versus photon penetration through brain tissue, again with the 30 mm s-d separation. Sensitivity increases approximately linearly with increasing photon penetration in the brain, with 83% of the variance in cerebral sensitivity explained by changes in photon penetration through the brain.
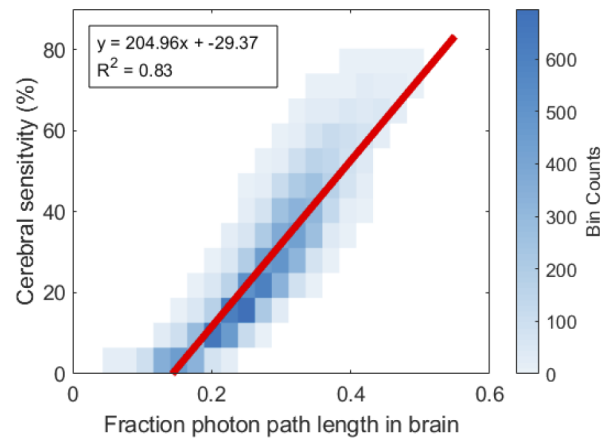
Fig. 9. Cerebral sensitivity versus the photon penetration through brain tissue at 30 mm.

Figure 10 shows superimposed plots of cerebral sensitivity and photon penetration through the brain versus s-d separation. We see that sensitivity increases approximately exponentially with s-d distance between 5-25 mm, and approximately linearly between 25- and 40-mm. Photon penetration through the brain increases approximately linearly between 5 and 30 mm, and begins to level off afterward.
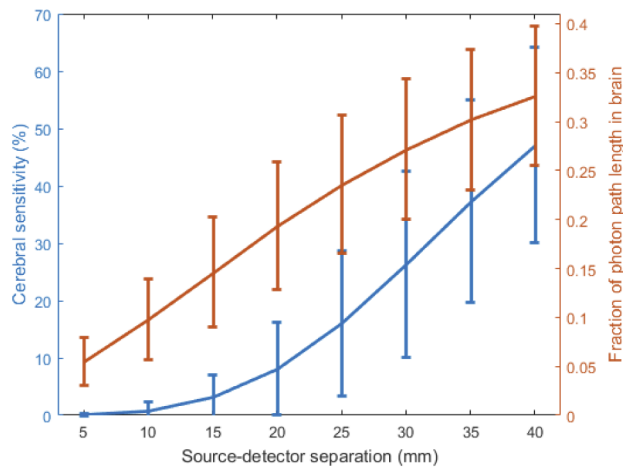

Fig. 10. Cerebral sensitivity and photon brain penetration versus source-detector separation.

3.3. Measurable correlates of cerebral sensitivity

Figure 11 shows the relationship between scalp and cerebral sensitivity for the 30 mm s-d separation. As described above, scalp sensitivity is defined as the percentage of observed decrease in long s-d separation BF_i from a 50% decrease in scalp blood flow, giving an estimate of how sensitive the detectors are to extracerebral fluctuations in blood flow. An almost perfect correlation is observed between the two metrics, with an R^2 value close to 1 when least squares regression is performed.

Figure 12 shows the ratio of cerebral to scalp sensitivity at the long s-d distances. As mentioned before, high levels of cerebral sensitivity and low levels of scalp sensitivity are desired for accurate
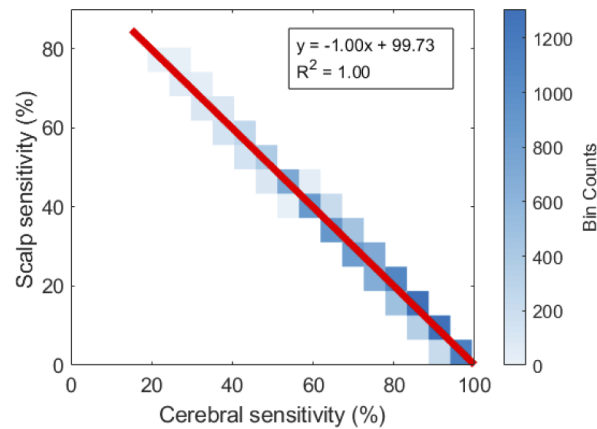
Fig. 11. Scalp versus cerebral sensitivity at 30 mm.

CBF measurements; thus, this metric is positively related to the desired cerebral sensitivity and negatively related to the undesired contamination sensitivity. We note that the ratio itself increases with s-d separation, showing that longer separations will afford higher proportions of the desired cerebral signal versus extracerebral contamination from physiological fluctuations.
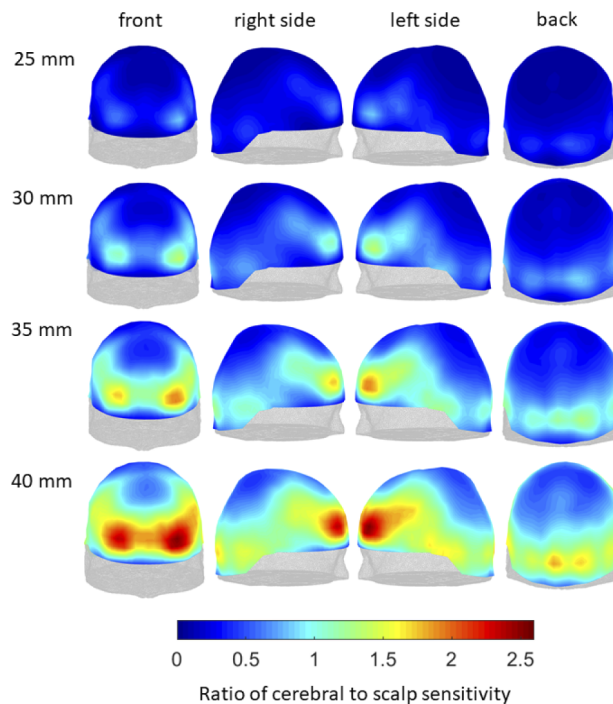

Fig. 12. Ratio of cerebral to scalp sensitivity for the four longer s-d distances.

.

Figure 13 displays the ratio of the 30 mm baseline BF_i to 5 mm baseline BF_i versus cerebral sensitivity across all subjects and all sensitivity locations. At ratios above 1, where the measured

30 mm BF_i is higher than the measured 5 mm BF_i, 70% of the data points contained cerebral sensitivities above 40%.
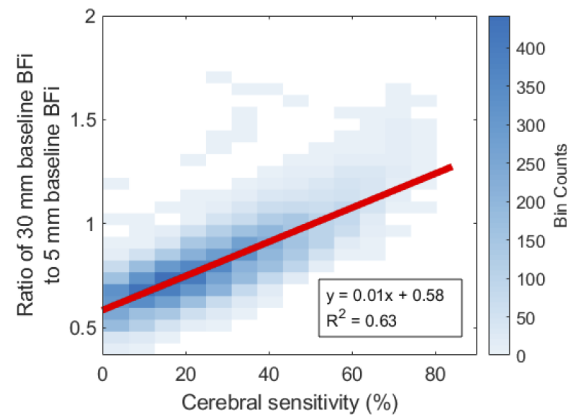

Fig. 13. Ratio of long-separation (30 mm) baseline BF_i to short-separation (5 mm) baseline BF_i versus cerebral sensitivity. A moderate R^2 value is observed.

4.   Discussion

4.1.   *Cerebral sensitivity and extracerebral thickness variations across the head*

A consistent sensitivity pattern is observed across subjects, where the front and occipital area of the head show high sensitivity, and the crown of the head demonstrates low sensitivity. This pattern is reflected analogously in the maps of extracerebral thickness, where we can observe a high distance-to-brain near the crown of the head (the area of low cerebral sensitivity), and a lower distance-to-brain elsewhere. The correlation between the two is confirmed with the least squares regression performed on sensitivity versus extracerebral thickness (Fig. 7). We note briefly that the subjects were lying supine in the MRI scanner when the images were taken, which may slightly affect the distance-to-brain calculations in the forehead or occipital areas (if the brain is closer to the occipital bone in supine position versus orthostatic); however, subjects will likely be in a similar position for DCS clinical neuromonitoring. While the sensitivity pattern itself seems fairly generalizable across subjects, the absolute cerebral sensitivity is not. We see, particularly in Fig. 4, that all subjects display similar sensitivity patterns, but the absolute cerebral sensitivity between subjects on a given area of the head is highly variable. Moreover, this high variability is not limited to cross-sex comparison, as we note that subjects 1 and 5 are both female yet have very low and high absolute sensitivity, respectively. Despite this, the consistent sensitivity map still shows that optimal DCS probe placement for an arbitrary subject lies either on the lateral sides of the forehead (relevant to traditional measurements), or in the occipital area of the head. These surfaces correspond to the frontal and occipital lobes of the brain, respectively.

Aside from this, we also observe some degree of asymmetry in the sensitivity maps: the right occipital area shows higher sensitivity than the left, whereas the left frontal area shows higher sensitivity than the right. This asymmetry can be noticed in the 35- and 40-mm sensitivity maps in Fig. 3 (average sensitivity across all subjects), and is also emphasized in Fig. 4, example subjects 4 (occipital area) and 5 (frontal area). The maps of extracerebral distance can also explain this asymmetry, as the right occipital area tends to have a lower distance-to-brain (particularly visible in the "male" and "all" subject rows in Fig. 6), along with the left frontal areas (particularly visible in the "male" row, Fig. 6). While this observation is primarily visual (robust testing may be

difficult due to small sample sizes and inter-subject variability), this asymmetry in scalp-to-cortex distance has been previously reported in literature and will be discussed in the next section. In summary, DCS measurements acquired on the left side of the forehead, or the right occipital area, may show higher sensitivity than their lateral counterparts. However, as mentioned previously, the degree of sensitivity improvement will be affected by the observed inter-subject variability in scalp-to-cortex patterns and absolute sensitivity maps.

We note that absolute cerebral sensitivity is limited at short s-d distances. In particular, on average less than 50% of the CBF increase will be captured at s-d distances less than 30 mm. For our study, no noise was added to the simulated DCS autocorrelations, and so this estimate does not account for noise or other artifacts which may occur during experimental measurements. As such, the sensitivity calculations do not provide an estimate of signal- or contrast-to-noise ratio – while cerebral sensitivity increases with s-d separation, so will measurement noise, and so real DCS applications will likely require s-d separations shorter than 40 mm. Still, we note from Fig. 12, which compares the ratio of brain to scalp, that the expected proportion of cerebral signal to extracerebral contamination increases with s-d distance. Because systemic physiological changes have been shown to contaminate the desired brain signal even at s-d distances of 30 mm [47], large-scale application of DCS for clinical neuromonitoring and otherwise will likely depend on hardware developments for improved signal-to-noise ratio (SNR), contrast-to-noise ratio (CNR), and depth sensitivity for longer s-d separations. Several approaches are indeed being explored to improve the fundamental DCS measurement SNR [20,25,26,28,48]. Further, algorithmic advances can be beneficial to isolate brain perfusion changes from extracerebral contamination [42,47,49–51].

In our study, females showed higher cerebral sensitivity than males, with the maximum average sensitivity 12% higher in females, along with a greater area of high sensitivity on the surface of the head. This is likely explained through observed differences in extracerebral thickness, where the maximum average thickness was approximately 4 mm lower for females. However, the p-value obtained from the Kruskal-Wallis test using spatial sensitivity averages for each subject does not reject the null hypothesis (that the data came from the same distribution) at a 5% significance level; the analogous test with spatial extracerebral thicknesses rejects the null hypothesis at a 5% significance level but not at a 1% significance level. As there is a high discrepancy in the sample size between females and males, as well as low overall sample size, more investigation is likely needed for generalizable results comparing sex differences in sensitivity and scalp-to-cortex distance.

4.2. Comparison to reported literature

The variation shown in the average extracerebral thickness across subjects matches several other studies. Perdue et al. has observed that the thinnest extracerebral thickness lies in a ring around the head above the ears, similar to our findings. Moreover, while studies by Beauchamp et al. and Whiteman et al. investigated scalp-to-cortex distance specifically in children [33,52], both also observed high extracerebral thickness at the crown of the heads, with lower scalp-to-cortex distance in the ring surrounding the crown. Last, a recent study by Fu et al. investigating scalp-to-cortex distance, primarily in infancy, included MRI analysis of adults 20-24 years of age [53], and showed similar scalp-to-cortex maps as our results and the aforementioned studies. With regards to the scalp-to-cortex asymmetry in the frontal and occipital areas, a skull thickness study by LeMay using X-rays of over 100 adult subjects shows similar observations of consistent left occipital and right frontal protrusions in the skull [54]. Both Beauchamp et al. and Whiteman et al. also noted the same phenomenon in children, which matches our analyses of extracerebral thickness. However, our observed differences in scalp-to-cortex distance between females and males do not match with those reported in Whiteman et al.'s study of scalp-to-cortex distances in 5- to 11-year-old children, though the subject population in the latter is of a markedly different

age group. Whiteman et al. showed an overall 3 mm increase in scalp-to-cortex distance in female subjects compared to males for most regions, which contrasts our results. We note that our study was conducted with few males (n = 4) compared to females (n = 12), in addition to limited combined sample size (n = 16). While there are extensive literature reports comparing skull and extracerebral anatomies between males and females, due to our limited sample size and male/female sample discrepancy we refrain from making robust comparisons of our results to literature observations.

While there has not been literature reported on DCS sensitivity variability across the head, we can compare the overall observed pattern to previous studies that performed similar analyses on NIRS sensitivity. Strangman et al. performed a study in 2014 mapping NIRS sensitivity across the entire Colin27 brain template, and found like patterns (low sensitivity at the crown of the head and higher sensitivity in the ring surrounding) [30]. Investigations by Cai et al. and Whiteman et al. have focused on children as opposed to adults, but have also showed the same phenomenon [32,33]. This is expected, because both NIRS and DCS employ near-infrared optical techniques which are inherently sensitive to superficial layers of tissue. Indeed, comparison of Fig. 10 showing photon penetration through brain tissue versus s-d separation to another study by Strangman et al. reveals very similar patterns, with penetration increasing approximately linearly from 20-35 mm, and beginning to level off afterward [31]. Since these NIRS studies typically employ the fraction of total photon pathlength in the brain or related metrics to define cerebral sensitivity, direct comparisons of their work with our sensitivity results is difficult; however, Selb et al. showed higher cerebral sensitivity (calculated as ratio of measured change over true physiological change) in DCS compared to NIRS, using Monte Carlo simulations at four forehead locations with an MRI volume in a 2014 study [34].

4.3. Measurable correlates of cerebral sensitivity

Scalp sensitivity is almost perfectly anti-correlated with cerebral sensitivity. While cerebral sensitivity itself can be difficult to assess in practice (as changes in CBF must be first induced in the subject, preferably monitored with some alternate method to gauge the exact increase or decrease), a pressure modulation maneuver put forward by Mesquita et al. may be able to give an estimate of cerebral sensitivity at a given location [55]. Briefly, scalp blood flow can be reduced by applying slight pressure on top of the DCS probe or tightening a tourniquet around the head just below the probe [56]. The amount of decrease observed in the long s-d separation BF_i is indicative of the degree of superficial contamination in the desired cerebral signal. In practice, an experimenter may be able to estimate differences in cerebral sensitivity across a given subject head by repeating this procedure in several different locations, and selecting the area where the long s-d separation BF_i decreases the least for a given reduction in scalp blood flow (monitored using measurements at short separation, e.g. 5 mm). While the procedure requires consistent modulations of scalp blood flow across the head, DCS instruments equipped with software that can display real-time traces of BF_i should allow for approximately consistent scalp blood flow reductions.

The second measurable estimate, while less directly correlated, may be easier to measure (again using a real-time BF_i calculation software interface). The baseline ratio of the long-separation BF_i to short-separation BF_i is moderately correlated with cerebral sensitivity – this is expected, since detectors that are probing more of the brain will also be detecting greater amounts of CBF compared to scalp blood flow. Since there is higher blood flow in the brain compared to the scalp [44], detectors with higher sensitivity to the brain should also have higher baseline BF_i values (up until scalp blood flow contamination becomes negligible). The short separation detectors quantify only the scalp blood flow, and so the ratio of long-separation BF_i to short-separation BF_i can be considered a proxy for the amount of CBF versus scalp blood flow detected. In

practice, an experimenter may simply place the probe on different locations of the head surface and observe the said ratio; areas with a higher ratio will likely feature higher cerebral sensitivity.

4.4. Limitations of study

In this study, we used MRIs from sixteen adult human subjects to map DCS cerebral sensitivity across the entire human head. Our investigation is mainly limited by the recruited subject population: the age of the subjects ranged from 25-41 years, with the average age being 29 years. Previous literature has reported skull growth to continue into late teenage years [57], and there is additional evidence that scalp-to-cortex distance increases heterogeneously across the head with age [58]. Thus, the observed cerebral sensitivity patterns should be generalized with caution outside of our subject age range. In general, we can expect DCS cerebral sensitivity to be higher in children and adolescents, due to the thinner skull and subsequent increased photon penetration in brain tissue, and lower in older populations, due to the increased scalp-to-cortex distance. From the findings of Whiteman et al. of extracerebral thickness patterns and NIRS sensitivity in children [33], we can expect our reported DCS cerebral sensitivity patterns to also be observed in younger populations, although the exact quantification still remains to be studied. Because of the heterogeneous nature of age-related increases in scalp-to-cortex distances, DCS cerebral sensitivity maps may be different in older subject populations, and may be worth further investigation.

Second, because our study used simulated, noiseless data, we cannot give estimates of SNR or CNR. As mentioned in section 4.1, although cerebral sensitivity increases with s-d separation, so will noise, and so the quality of experimental signals of the brain with increasing s-d separation will likely be different than what is initially reported here. However, the noise levels will primarily depend on s-d separation and not head location, unlike the cerebral sensitivity itself – the spatial and inter-subject variations of the latter are the focus of this study and are not dependent on noise levels. Nevertheless, two computational approaches which improve cerebral sensitivity are relevant to discuss here. First, this study used the entire g_2 curve to calculate BF_i, whereas Selb et al. have observed that restricting the BF_i fit to only the early delays improves cerebral sensitivity [34]. Even so, our previous work has shown that while absolute cerebral sensitivity increases when restricting the fit to early delay times, the sensitivity to noise increases as well [47]. While the increase in absolute cerebral sensitivity was briefly verified with the cerebral sensitivity maps of several example subjects (data not shown), we did not observe any qualitative difference in the cerebral sensitivity pattern itself, and therefore our final conclusions regarding the spatial distribution of favorable measurement areas remain unchanged. On the other hand, the effect of early delay fitting on noise sensitivity requires the incorporation of the noise model into our simulated data to fairly assess potential benefits; thus, the optimal g_2 fitting range from a CNR perspective should be a point of future investigation. Second, there have been several previous studies (including by our own group) investigating the effect of using a layered model to fit DCS data [42,47,49,59]. Such models show improved accuracy in isolating cerebral blood flow from scalp hemodynamics; however, our previous work again shows that sensitivity to noise increases with the multi-layer model [47]. Incorporating noise into the simulated data would again be needed to investigate the CNR effects of multi-layered models and the likelihood of real-world benefits.

Recent work by others in our group have performed DCS SNR investigations with both simulations and *in-vivo* [34,48,60]. In practice, DCS measurements do not usually exceed s-d separations of over 30 mm [1,2], although recently measurements with 35 mm s-d separation have been published using massive multi-speckle detection or long-wavelength (1064 nm) operation [20,48]. As mentioned previously, attaining the cerebral sensitivity estimated at the longer s-d separations shown in this work (35 and 40 mm) will likely require hardware advances in DCS technology compared to the devices currently used for human subject research. The next steps

for this study would involve experimental verification of the sensitivity mapping shown here, which would allow for realistic estimates of sensitivity variations throughout the head, along with SNR/CNR evaluations for measurements at different s-d separations.

5. Conclusion

We mapped DCS cerebral sensitivity across the adult human head using MRI scans from sixteen adult human subjects. Significant variations in cerebral sensitivity were found, which are primarily attributable to changes in extracerebral thickness. Areas of high sensitivity include the lateral sides of the forehead and occipital area of the head, although sensitivity levels themselves will vary across subjects. Measurable correlates of cerebral sensitivity include scalp sensitivity and the ratio between long- and short-separation baseline BF_i values. Such information is valuable for optimizing DCS probe placement in clinical neuromonitoring settings, and would be informative for any functional DCS studies. Future directions for this work include experimental verification of the simulated results in adult human subjects, incorporating SNR and CNR metrics, and extending sensitivity mapping to children or older populations.

Disclosures. MAF has a financial interest in 149 Medical, Inc., a company developing DCS technology for assessing and monitoring cerebral blood flow in newborn infants. MAF's interests were reviewed and are managed by Massachusetts General Hospital and Mass General Brigham in accordance with their conflict of interest policies (I).

Data availability. Data underlying the results presented in this paper are not publicly available at this time but may be obtained from the authors upon reasonable request.

References

1. T. Durduran and A. G. Yodh, "Diffuse correlation spectroscopy for non-invasive, micro-vascular cerebral blood flow measurement," Neuroimage **85**(0 1), 51–63 (2014).
2. E. M. Buckley, A. B. Parthasarathy, P. E. Grant, A. G. Yodh, and M. A. Franceschini, "Diffuse correlation spectroscopy for measurement of cerebral blood flow: future prospects," *Neurophotonics* (2014).
3. R. C. Mesquita, T. Durduran, G. Yu, E. M. Buckley, M. N. Kim, C. Zhou, R. Choe, U. Sunar, and A. G. Yodh, "Direct measurement of tissue blood flow and metabolism with diffuse optics," Philosophical Transactions of the Royal Society A: Mathematical, Physical and Engineering Sciences **369**(1955), 4390–4406 (2011).
4. A. I. Zavriyev, K. Kaya, P. Farzam, P. Y. Farzam, J. Sunwoo, A. S. Jassar, T. M. Sundt, S. A. Carp, M. A. Franceschini, and J. Z. Qu, "The role of diffuse correlation spectroscopy and frequency-domain near-infrared spectroscopy in monitoring cerebral hemodynamics during hypothermic circulatory arrests," JTCVS Tech **7**, 161–177 (2021).
5. W. B. Baker, R. Balu, L. He, V. C. Kavuri, D. R. Busch, O. Amendolia, F. Quattrone, S. Frangos, E. Maloney-Wilensky, K. Abramson, E. Mahanna Gabrielli, A. G. Yodh, and W. Andrew Kofke, "Continuous non-invasive optical monitoring of cerebral blood flow and oxidative metabolism after acute brain injury," J Cereb Blood Flow Metab **39**(8), 1469–1485 (2019).
6. D. R. Busch, R. Balu, W. B. Baker, W. Guo, L. He, M. Diop, D. Milej, V. Kavuri, O. Amendolia, K. St. Lawrence, A. G. Yodh, and W. A. Kofke, "Detection of brain hypoxia based on noninvasive optical monitoring of cerebral blood flow with diffuse correlation spectroscopy," Neurocrit Care **30**(1), 72–80 (2019).
7. L. He, W. B. Baker, D. Milej, V. C. Kavuri, R. C. Mesquita, D. R. Busch, K. Abramson, J. Y. Jiang, M. Diop, K. S. Lawrence, O. Amendolia, F. Quattrone, R. Balu, W. A. Kofke, and A. G. Yodh, "Noninvasive continuous optical monitoring of absolute cerebral blood flow in critically ill adults," NPh **5**(4), 045006 (2018).
8. M. N. Kim, T. Durduran, S. Frangos, B. L. Edlow, E. M. Buckley, H. E. Moss, C. Zhou, G. Yu, R. Choe, E. Maloney-Wilensky, R. L. Wolf, M. S. Grady, J. H. Greenberg, J. M. Levine, A. G. Yodh, J. A. Detre, and W. A. Kofke, "Noninvasive Measurement of Cerebral Blood Flow and Blood Oxygenation Using Near-Infrared and Diffuse Correlation Spectroscopies in Critically Brain-Injured Adults," Neurocrit Care **12**(2), 173–180 (2010).
9. M. N. Kim, B. L. Edlow, T. Durduran, S. Frangos, R. C. Mesquita, J. M. Levine, J. H. Greenberg, A. G. Yodh, and J. A. Detre, "Continuous optical monitoring of cerebral hemodynamics during head-of-bed manipulation in brain-injured adults," Neurocrit. Care **20**(3), 443–453 (2014).
10. C.-S. Poon, B. Rinehart, D. S. Langri, T. M. Rambo, A. J. Miller, B. Foreman, and U. Sunar, "Noninvasive Optical Monitoring of Cerebral Blood Flow and EEG Spectral Responses after Severe Traumatic Brain Injury: A Case Report," Brain Sci **11**(8), 1093 (2021).

11. J. Selb, K.-C. Wu, J. Sutin, P.-Y. I. Lin, P. Farzam, S. Bechek, A. Shenoy, A. B. Patel, D. A. Boas, M. A. Franceschini, and E. S. Rosenthal, "Prolonged monitoring of cerebral blood flow and autoregulation with diffuse correlation spectroscopy in neurocritical care patients," Neurophotonics **5**(04), 1 (2018).

12. T. Durduran, C. Zhou, B. L. Edlow, G. Yu, R. Choe, M. N. Kim, B. L. Cucchiara, M. E. Putt, Q. Shah, S. E. Kasner, J. H. Greenberg, A. G. Yodh, and J. A. Detre, "Transcranial Optical Monitoring of Cerebrovascular Hemodynamics in Acute Stroke Patients," Opt. Express, OE **17**(5), 3884–3902 (2009).

13. C. G. Favilla, R. M. Forti, A. Zamzam, J. A. Detre, M. T. Mullen, A. G. Yodh, S. E. Kasner, D. R. Busch, W. B. Baker, R. C. Mesquita, D. Kung, and S. R. Messé, "Perfusion Enhancement with Respiratory Impedance After Stroke (PERI-Stroke)," Neurotherapeutics **16**(4), 1296–1303 (2019).

14. C. Gregori-Pla, I. Blanco, P. Camps-Renom, P. Zirak, I. Serra, G. Cotta, F. Maruccia, L. Prats-Sánchez, A. Martínez-Domeño, D. R. Busch, G. Giacalone, J. Martí-Fàbregas, T. Durduran, and R. Delgado-Mederos, "Early microvascular cerebral blood flow response to head-of-bed elevation is related to outcome in acute ischemic stroke," J Neurol **266**(4), 990–997 (2019).

15. K.-C. Wu, J. Sunwoo, F. Sheriff, P. Farzam, P. Y. Farzam, F. Orihuela-Espina, S. L. LaRose, A. D. Monk, M. A. Aziz-Sultan, N. Patel, H. Vaitkevicius, and M. A. Franceschini, "Validation of diffuse correlation spectroscopy measures of critical closing pressure against transcranial Doppler ultrasound in stroke patients," J Biomed Opt **26**(3), 036008 (2021).

16. P. Zirak, C. Gregori-Pla, I. Blanco, A. F. M.d, G. Cotta, P. Bramon, I. Serra, A. M. M.d, J. Solà-Soler, B. F. Giraldo-Giraldo, T. Durduran, and M. Mayos, "Characterization of the microvascular cerebral blood flow response to obstructive apneic events during night sleep," NPh **5**(4), 045003 (2018).

17. C. Gregori-Pla, R. C. Mesquita, C. G. Favilla, D. R. Busch, I. Blanco, P. Zirak, L. K. Frisk, S. Avtzi, F. Maruccia, G. Giacalone, G. Cotta, P. Camps-Renom, M. T. Mullen, J. Martí-Fàbregas, L. Prats-Sánchez, A. Martínez-Domeño, S. E. Kasner, J. H. Greenberg, C. Zhou, B. L. Edlow, M. E. Putt, J. A. Detre, A. G. Yodh, T. Durduran, and R. Delgado-Mederos, "Blood flow response to orthostatic challenge identifies signatures of the failure of static cerebral autoregulation in patients with cerebrovascular disease," BMC Neurol. **21**(1), 154 (2021).

18. G. M. Tellis, R. C. Mesquita, and A. G. Yodh, "Use of diffuse correlation spectroscopy to measure brain blood flow differences during speaking and nonspeaking tasks for fluent speakers and persons who stutter," Perspectives on Fluency and Fluency Disorders **21**(3), 96–106 (2011).

19. T. Durduran, G. Yu, M. G. Burnett, J. A. Detre, J. H. Greenberg, J. Wang, C. Zhou, and A. G. Yodh, "Diffuse optical measurement of blood flow, blood oxygenation, and metabolism in a human brain during sensorimotor cortex activation," Opt Lett **29**(15), 1766–1768 (2004).

20. W. Zhou, O. Kholiqov, J. Zhu, M. Zhao, L. L. Zimmermann, R. M. Martin, B. G. Lyeth, and V. J. Srinivasan, "Functional interferometric diffusing wave spectroscopy of the human brain," Sci. Adv. **7**(20), eabe0150 (2021).

21. J. A. N. Fisher, I. Gumenchuk, O. S. Rogovin, A. G. Yodh, and D. R. Busch, "Asymmetric, dynamic adaptation in prefrontal cortex during dichotic listening tasks," NPh **7**(4), 045008 (2020).

22. J. Li, C.-S. Poon, J. Kress, D. J. Rohrbach, and U. Sunar, "Resting-state functional connectivity measured by diffuse correlation spectroscopy," J Biophotonics **11**(2), e201700165 (2018).

23. K. Murali and H. M. Varma, "Multi-speckle diffuse correlation spectroscopy to measure cerebral blood flow," Biomed. Opt. Express BOE **11**(11), 6699–6709 (2020).

24. J. Sutin, B. Zimmerman, D. Tyulmankov, D. Tamborini, K. C. Wu, J. Selb, A. Gulinatti, I. Rech, A. Tosi, D. A. Boas, and M. A. Franceschini, "Time-domain diffuse correlation spectroscopy," Optica OPTICA **3**(9), 1006–1013 (2016).

25. S. A. Carp, D. Tamborini, D. Mazumder, K.-C. Tony Wu, M. R. Robinson, K. A. Stephens, O. Shatrovoy, N. Lue, N. Ozana, M. H. Blackwell, and M. A. Franceschini, "Diffuse correlation spectroscopy measurements of blood flow using 1064 nm light," J Biomed Opt **25**(9), 097003 (2020).

26. M. B. Robinson, D. A. Boas, S. Sakadžic, M. A. Franceschini, and S. A. Carp, "Interferometric diffuse correlation spectroscopy improves measurements at long source–detector separation and low photon count rate," JBO **25**(9), 097004 (2020).

27. M. B. Robinson, S. A. Carp, A. Peruch, D. A. Boas, M. A. Franceschini, and S. Sakadžić, "Characterization of continuous wave ultrasound for acousto-optic modulated diffuse correlation spectroscopy (AOM-DCS)," Biomed Opt Express **11**(6), 3071–3090 (2020).

28. W. Liu, R. Qian, S. Xu, P. Chandra Konda, J. Jönsson, M. Harfouche, D. Borycki, C. Cooke, E. Berrocal, Q. Dai, H. Wang, and R. Horstmeyer, "Fast and sensitive diffuse correlation spectroscopy with highly parallelized single photon detection," APL Photonics **6**(2), 026106 (2021).

29. N. J. Davis, "Variance in cortical depth across the brain surface: Implications for transcranial stimulation of the brain," European Journal of Neuroscience **53**(4), 996–1007 (2021).

30. G. E. Strangman, Q. Zhang, and Z. Li, "Scalp and skull influence on near infrared photon propagation in the Colin27 brain template," *NeuroImage* (2014).

31. G. E. Strangman, Z. Li, and Q. Zhang, "Depth sensitivity and source-detector separations for near infrared spectroscopy based on the Colin27 Brain Template," PLoS One **8**(8), e66319 (2013).

32. L. Cai, T. Nitta, S. Yokota, T. Obata, E. Okada, and H. Kawaguchi, "Targeting brain regions of interest in functional near-infrared spectroscopy—Scalp-cortex correlation using subject-specific light propagation models," Human Brain Mapping **42**(7), 1969–1986 (2021).

33. A. C. Whiteman, H. Santosa, D. F. Chen, S. Perlman, and T. Huppert, "Investigation of the sensitivity of functional near-infrared spectroscopy brain imaging to anatomical variations in 5- to 11-year-old children," Neurophotonics **5**(1), 011009 (2018).

34. J. Selb, D. A. Boas, S.-T. Chan, K. C. Evans, E. M. Buckley, and S. A. Carp, "Sensitivity of near-infrared spectroscopy and diffuse correlation spectroscopy to brain hemodynamics: simulations and experimental findings during hypercapnia," Neurophotonics **1**(1), 015005 (2014).

35. B. Fischl, "FreeSurfer," Neuroimage **62**(2), 774–781 (2012).

36. K. L. Perdue and S. G. Diamond, "T1 magnetic resonance imaging head segmentation for diffuse optical tomography and electroencephalography," J Biomed Opt **19**(2), 026011 (2014).

37. A. P. Tran, S. Yan, and Q. Fang, "Improving model-based functional near-infrared spectroscopy analysis using mesh-based anatomical and light-transport models," Neurophotonics **7**(1), 015008 (2020).

38. Qianqian Fang and D. A. Boas, "Tetrahedral mesh generation from volumetric binary and grayscale images," in *2009 IEEE International Symposium on Biomedical Imaging: From Nano to Macro* (IEEE, 2009), pp. 1142–1145.

39. Q. Fang, "Mesh-based Monte Carlo method using fast ray-tracing in Plücker coordinates," Biomed. Opt. Express, BOE **1**(1), 165–175 (2010).

40. V. Jurcak, D. Tsuzuki, and I. Dan, "10/20, 10/10, and 10/5 systems revisited: their validity as relative head-surface-based positioning systems," Neuroimage **34**(4), 1600–1611 (2007).

41. Q. Fang and S. Yan, "Graphics processing unit-accelerated mesh-based Monte Carlo photon transport simulations," JBO **24**(11), 115002 (2019).

42. L. Gagnon, M. Desjardins, J. Jehanne-Lacasse, L. Bherer, and F. Lesage, "Investigation of diffuse correlation spectroscopy in multi-layered media including the human head," Opt. Express **16**(20), 15514 (2008).

43. D. A. Boas, S. Sakadžic, J. Selb, P. Farzam, M. A. Franceschini, and S. A. Carp, "Establishing the diffuse correlation spectroscopy signal relationship with blood flow," Neurophotonics **3**(3), 031412 (2016).

44. E. Ohmae, Y. Ouchi, M. Oda, T. Suzuki, S. Nobesawa, T. Kanno, E. Yoshikawa, M. Futatsubashi, Y. Ueda, H. Okada, and Y. Yamashita, "Cerebral hemodynamics evaluation by near-infrared time-resolved spectroscopy: Correlation with simultaneous positron emission tomography measurements," NeuroImage **29**(3), 697–705 (2006).

45. C. J. Holmes, R. Hoge, L. Collins, R. Woods, A. W. Toga, and A. C. Evans, "Enhancement of MR images using registration for signal averaging," J Comput Assist Tomogr **22**(2), 324–333 (1998).

46. Luigi Giaccari, *Surface Reconstruction from Scattered Points Cloud* (*Open Surfaces*) (n.d.).

47. M. M. Wu, S.-T. Chan, D. Mazumder, D. Tamborini, K. A. Stephens, B. Deng, P. Farzam, J. Y. Chu, M. A. Franceschini, J. Z. Qu, and S. A. Carp, "Improved accuracy of cerebral blood flow quantification in the presence of systemic physiology cross-talk using multi-layer Monte Carlo modeling," Neurophotonics **8**(1), 015001 (2021).

48. N. Ozana, A. I. Zavriyev, D. Mazumder, M. Robinson, K. Kaya, M. Blackwell, S. A. Carp, and M. A. Franceschini, "Superconducting nanowire single-photon sensing of cerebral blood flow," Neurophotonics **8**(03), 035006 (2021).

49. K. Verdecchia, M. Diop, A. Lee, L. B. Morrison, T.-Y. Lee, and K. St. Lawrence, "Assessment of a multi-layered diffuse correlation spectroscopy method for monitoring cerebral blood flow in adults," Biomed. Opt. Express **7**(9), 3659 (2016).

50. J. Li, G. Dietsche, D. Iftime, S. E. Skipetrov, G. Maret, T. Elbert, B. Rockstroh, and T. Gisler, "Noninvasive detection of functional brain activity with near-infrared diffusing-wave spectroscopy," J. Biomed. Opt. **10**(4), 044002 (2005).

51. W. B. Baker, A. B. Parthasarathy, T. S. Ko, D. R. Busch, K. Abramson, S.-Y. Tzeng, R. C. Mesquita, T. Durduran, J. H. Greenberg, D. K. Kung, and A. G. Yodh, "Pressure modulation algorithm to separate cerebral hemodynamic signals from extracerebral artifacts," Neurophotonics **2**(3), 035004 (2015).

52. M. S. Beauchamp, M. R. Beurlot, E. Fava, A. R. Nath, N. A. Parikh, Z. S. Saad, H. Bortfeld, and J. S. Oghalai, "The Developmental Trajectory of Brain-Scalp Distance from Birth through Childhood: Implications for Functional Neuroimaging," PLOS ONE **6**(9), e24981 (2011).

53. X. Fu and J. E. Richards, "Investigating developmental changes in scalp-to-cortex correspondence using diffuse optical tomography sensitivity in infancy," NPh **8**(3), 035003 (2021).

54. M. LeMay, "Asymmetries of the skull and handedness: Phrenology revisited," J. Neurol. Sci. **32**(2), 243–253 (1977).

55. R. C. Mesquita, S. S. Schenkel, D. L. Minkoff, X. Lu, C. G. Favilla, P. M. Vora, D. R. Busch, M. Chandra, J. H. Greenberg, J. A. Detre, and A. G. Yodh, "Influence of probe pressure on the diffuse correlation spectroscopy blood flow signal: extra-cerebral contributions," Biomed Opt Express **4**(7), 978–994 (2013).

56. D. Milej, A. Abdalmalak, A. Rajaram, and K. S. Lawrence, "Direct assessment of extracerebral signal contamination on optical measurements of cerebral blood flow, oxygenation, and metabolism," NPh **7**(4), 045002 (2020).

57. H. T. Epstein, "Phrenoblysis: Special brain and mind growth periods. I. Human brain and skull development," Developmental Psychobiology **7**(3), 207–216 (1974).

58. H. Lu, S. S. M. Chan, and L. C. W. Lam, "Localized analysis of normalized distance from scalp to cortex and personalized evaluation (LANDSCAPE): focusing on age- and dementia-specific changes," J Alzheimers Dis **67**(4), 1331–1341 (2019).

59. H. Zhao, E. Sathialingam, and E. M. Buckley, "Accuracy of diffuse correlation spectroscopy measurements of cerebral blood flow when using a three-layer analytical model," Biomed Opt Express **12**(11), 7149–7161 (2021).
60. D. Mazumder, M. M. Wu, N. Ozana, D. Tamborini, M. A. Franceschini, and S. A. Carp, "Optimization of time domain diffuse correlation spectroscopy parameters for measuring brain blood flow," NPh **8**(3), 035005 (2021).